Journal of Computational Physics 514 (2024) 113260

Contents lists available at ScienceDirect

Journal of Computational Physics

journal homepage: www.elsevier.com/locate/jcp

New implicit time integration schemes combining high frequency damping with high second order accuracy

Wulf G. Dettmer *, Eman Alhayki

Faculty of Science And Engineering, Swansea University, Bay Campus, Fabian Way, Swansea, SA1 8EN, Wales, United Kingdom

ARTICLE INFO

Keywords:
Implicit numerical time integration
Generalised-α method
Backward difference formulae
Unconditional stability
Accuracy

ABSTRACT

It is shown that weighted linear combinations of the generalised-α method and certain related higher order schemes allow for the formulation of unconditionally stable single step time integration methods with improved second order accuracy and more targeted high-frequency damping. It is also shown that, if the user controlled high frequency damping parameter ρ_∞ is set to zero, the new schemes can be expressed as linear multistep backward difference formulae and, in a particular case, recover Park's method. The performance of the proposed methods is illustrated in terms of mathematical analysis and a number of linear and nonlinear numerical examples including finite element based solutions of the incompressible Navier-Stokes equations.

1. Introduction

Implicit unconditionally stable time integration schemes are a crucial ingredient to the computer simulation of any dynamic physical process unless it is suitable for the employment of an explicit strategy. They are extensively used in computational fluid and solid dynamics. Presuming unconditional stability, which is a fundamental requirement for an implicit time integration scheme, the criteria for the assessment of the performance of a particular scheme are the approximation accuracy and the numerical damping characteristics. Due to the second Dahlquist barrier, see for instance [13], the methods can be only of first or second order accuracy and cannot exceed the accuracy of the trapezoidal rule. Yet, the trapezoidal rule does not feature any numerical damping and is therefore not suitable for many problems in fluid or solid dynamics, where unresolved high frequency responses must be suppressed.

An optimal implicit time integration scheme features second order accuracy with small absolute error values and a noticeable or even substantial amount of numerical damping in the high frequency regime. This behaviour is largely offered by the generalised-α method, which is available for applications in solid and fluid mechanics, as described in [7,14,16]. It provides user controlled high frequency damping combined with second order accuracy. Therefore, it has been successfully used in computational fluid dynamics (see [3,4,8,9,14,18,20] and many others), computational solid dynamics (see [7] and the vast number of citing articles), fluid-structure interaction ([5,10,11,15,17,22] and others), but also in phase field modelling [1,12,19], biomechanics [21], thermomechanics [27] and other application areas. For the limit values, zero and one, of the user controlled high frequency damping parameter ρ_∞, the generalised-α method as described in [14] coincides with a number of other schemes, including the Wilson/Houboldt scheme and the second order backward difference formula (BDF-2), as well as the trapezoidal rule (TR) and the Crank Nicolson scheme. Hence, the parameter ρ_∞ provides a mechanism to interpolate between the less accurate, dissipative BDF-2 method and the more accurate, but non-dissipative TR scheme. This is illustrated in Fig. 1.

* Corresponding author.
E-mail addresses: w.g.dettmer@swansea.ac.uk (W.G. Dettmer), e.s.h.j.alhayki@swansea.ac.uk (E. Alhayki).

https://doi.org/10.1016/j.jcp.2024.113260
Received 22 February 2024; Received in revised form 30 June 2024; Accepted 2 July 2024

Available online 8 July 2024

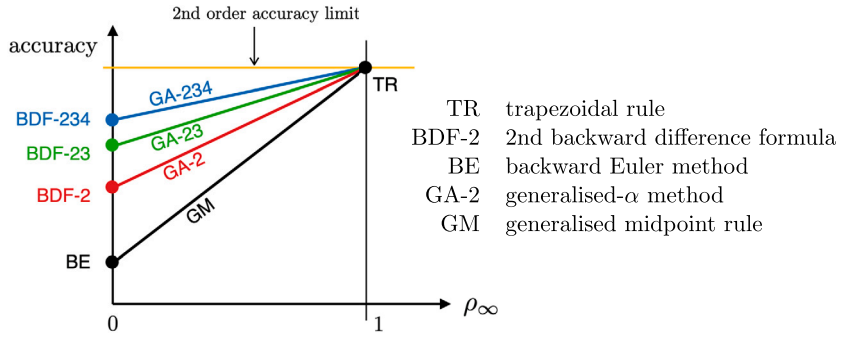

Fig. 1. Schematic overview of unconditionally stable implicit time integration schemes considered in this article; GA-23, GA-234, BDF-23 and BDF-234 are proposed in Sections 3 and 5; GM, GA-2, GA-23 and GA-234 can be regarded as interpolations between BDF methods and the trapezoidal rule. They require that the user sets the value of ρ_∞; $\rho_\infty = 0 \rightarrow$ strong high frequency damping, $\rho_\infty = 1 \rightarrow$ no high frequency damping. BDF-23 is equivalent to Park's method, see for instance [13,23].

In this work, new numerical time integration schemes are developed based on the generalised-α method, which maintain second order accuracy, unconditional stability and user controlled high frequency damping, but offer improved accuracy and more targeted high frequency damping, *i.e.* the onset of numerical damping is shifted more towards the regime of large time steps. For $\rho_\infty = 0$, the new schemes give rise to backward difference formulae, which, for a particular case, recover one of the BDF2OPT methods presented in [26]. This scheme is referred to as Park's method in [13], and it is particularly well suited for stiff problems in mechanics as argued in [23]. The relationship between the new methods, the generalised-α method and the BDF-2 and TR schemes is illustrated qualitatively in Fig. 1, in terms of accuracy and high frequency damping. As shown, the key contribution of the proposed methods is that they almost achieve the best possible second order accuracy, *i.e.* the accuracy of the trapezoidal rule, while still offering user controlled high frequency damping. The new methods are derived from weighted linear combinations of the original generalised-α method presented in [14] with generalised higher order schemes. The advantages offered by the new schemes are associated with negligible additional computational cost. The computer implementation in existing code is straightforward and only requires one or two more current state or history arrays.

For clarity, it is noted that the methods presented in this work require the solution of a single set of solution variables only. In this way they differ from those implicit schemes which are based on an augmented set of solution variables or require a sequence of system solutions. Such methods include the linear discontinuous finite element method in time, see [9] and references therein, implicit Runge-Kutta schemes or the composite scheme presented in [2]. Recently, a higher order generalised-α method has been proposed in [6] which maintains the desirable stability and damping properties but requires the computation of several sets of solution variables.

The remainder of this article is organised as follows: In Section 2, a family of higher order methods is presented which recovers the generalised-α method for the special case of second order accuracy. Unconditionally stable weighted linear combinations of the second, third and fourth order accurate schemes are proposed in Section 3, resulting in two new single step time integration methods. The properties of the new schemes are analysed in Section 4. In Section 5, it is shown that the new schemes give rise to backward difference formulae with higher accuracy than the standard second order formula. In Sections 6 to 8, the linear scalar oscillator and two finite element models of unsteady incompressible fluid flow are used to illustrate the performance of the proposed schemes. Conclusions are presented in Section 9.

2. A family of time integration schemes of order p

Consider the first order initial value problem

$$\dot{u}(t) \; - \; f\left(u(t), t\right) \; = \; 0 \qquad \text{with} \qquad u(0) = u_0 \, , \tag{1}$$

where u is the solution variable, t denotes time and $\dot{u} = \mathrm{d}u/\mathrm{d}t$. For the discussion of numerical time integration schemes, it is common practice to consider the special case of the scalar linear problem

$$\dot{u}(t) \; - \; \lambda \, u(t) \; = \; 0 \qquad \text{with} \qquad u(0) = u_0 \, , \tag{2}$$

where $\lambda = -\xi + i\,\omega$. The exact solution can be expressed as

$$u(t) \; = \; u_0 \, e^{\lambda \, t} \, . \tag{3}$$

Introducing the sequence of discrete time instants t_n with $n = 0, 1, 2, \ldots$ and the step size $\Delta t = t_{n+1} - t_n$ gives rise to the exact amplification factor

$$\zeta_{\text{exact}} \; = \; e^{\lambda \, \Delta t} \qquad \text{with} \qquad u_{n+1} \; = \; \zeta_{\text{exact}} \, u_n \, . \tag{4}$$

The set of equations

$$\dot{u}_{n+\beta} \; - \; \lambda \, u_{n+\alpha} \; = \; 0 \tag{5}$$

Table 1
Coefficients β_i for the family of time integration schemes GA-p.

p	β_0	β_1	β_2	β_3
2	$\frac{-\rho_\infty+3}{2(\rho_\infty+1)}$	$\frac{3\rho_\infty-1}{2(\rho_\infty+1)}$		
3	$\frac{2\rho_\infty^2-5\rho_\infty+11}{6(\rho_\infty+1)}$	$\frac{-2\rho_\infty^2+11\rho_\infty-5}{6(\rho_\infty+1)}$	$\frac{-\rho_\infty^2+\rho_\infty-1}{3(\rho_\infty+1)}$	
4	$\frac{-3\rho_\infty^3+7\rho_\infty^2-13\rho_\infty+25}{12(\rho_\infty+1)}$	$\frac{3\rho_\infty^3-7\rho_\infty^2+25\rho_\infty-13}{12(\rho_\infty+1)}$	$\frac{3\rho_\infty^3-7\rho_\infty^2+7\rho_\infty-7}{12(\rho_\infty+1)}$	$\frac{\rho_\infty^3-\rho_\infty^2+\rho_\infty-1}{4(\rho_\infty+1)^2}$

$$u_{n+\alpha} = \alpha\, u_{n+1} + (1-\alpha)\, u_n \tag{6}$$

$$\dot{u}_{n+\beta} = \beta_0\, \dot{u}_{n+1} + \sum_{i=1}^{p-1} \beta_i\, u_n^{(i)'}\, \Delta t^{i-1} \tag{7}$$

$$u_{n+1}^{(i)'} = u_n^{(i)'} + \Delta t \left(\gamma\, u_{n+1}^{(i+1)'} + (1-\gamma)\, u_n^{(i+1)'} \right) \quad \text{for} \quad i = 0, 1, 2, ..., p-2 \tag{8}$$

with $p \geq 2$ represents a family of implicit numerical time integration schemes. The term $u_n^{(i)'}$ denotes the i-th derivative of the variable u at the time instant t_n. The numerical properties of the schemes and the conditions for the scalar parameters α, β_i and γ are determined in the remainder of this section.

First, the associated amplification matrix $\mathbf{A}^{(p)}$ of the schemes is considered. It is defined by

$$\begin{Bmatrix} u_{n+1} \\ \dot{u}_{n+1}\,\Delta t \\ u_{n+1}^{(2)'}\,\Delta t^2 \\ u_{n+1}^{(3)'}\,\Delta t^3 \\ \cdots \\ u_{n+1}^{(p-1)'}\,\Delta t^{p-1} \end{Bmatrix} = \mathbf{A}^{(p)} \begin{Bmatrix} u_n \\ \dot{u}_n\,\Delta t \\ u_n^{(2)'}\,\Delta t^2 \\ u_n^{(3)'}\,\Delta t^3 \\ \cdots \\ u_n^{(p-1)'}\,\Delta t^{p-1} \end{Bmatrix}. \tag{9}$$

The matrix $\mathbf{A}^{(p)}$ is of dimension $p \times p$ and can be obtained from symbolic mathematical software. For $p = 4$, it can be written as

$$\mathbf{A}^{(4)} = \frac{1}{\delta} \begin{bmatrix} \delta + \gamma\lambda\Delta t & \beta_0\eta - \beta_1\gamma & -\beta_2\gamma & -\beta_3\gamma \\ \lambda\Delta t & \alpha\eta\lambda\Delta t - \beta_1 & -\beta_2 & -\beta_3 \\ \lambda\Delta t/\gamma & (\alpha\lambda\Delta t - \beta_0 - \beta_1)/\gamma & -(\delta\eta + \beta_2)/\gamma & -\beta_3/\gamma \\ \lambda\Delta t/\gamma^2 & (\alpha\lambda\Delta t - \beta_0 - \beta_1)/\gamma^2 & -(\delta + \beta_2)/\gamma^2 & -(\gamma\delta\eta + \beta_3)/\gamma^2 \end{bmatrix} \tag{10}$$

where $\delta = \beta_0 - \alpha\,\gamma\,\lambda\Delta t$ and $\eta = 1 - \gamma$. The amplification matrices $\mathbf{A}^{(2)}$ and $\mathbf{A}^{(3)}$ are equal to the two and three dimensional top left submatrices of $\mathbf{A}^{(4)}$, respectively.

Before the investigation of numerical accuracy, it is convenient to consider the high frequency damping behaviour of the schemes. The spectral radius of matrix $\mathbf{A}^{(p)}$ is

$$\rho\left(\mathbf{A}^{(p)}\right) = \max\left(|\zeta_i|\right), \tag{11}$$

where ζ_i with $i = 1, 2, ..., p$ are the eigenvalues of $\mathbf{A}^{(p)}$. Introducing the spectral radius ρ_∞ for an infinite time step, symbolic mathematical software renders

$$\rho_\infty = \lim_{\Delta t \to \infty} \rho\left(\mathbf{A}^{(p)}\right) = \max\left(\left| -\frac{1-\alpha}{\alpha} \right|, \left| -\frac{1-\gamma}{\gamma} \right| \right). \tag{12}$$

Setting

$$\alpha = \gamma = \frac{1}{1+\rho_\infty} \tag{13}$$

ensures that the absolute values of all eigenvalues converge to ρ_∞ as Δt tends to infinity. By keeping ρ_∞ as a free parameter, user controlled high frequency damping is enabled.

In order to assess the accuracy of the family of schemes defined by Equations (5) to (8), the amplification factor ζ_{exact} is inserted into the characteristic polynomial of $\mathbf{A}^{(p)}$ and the resulting expression expanded as a series of powers of Δt. Equating the first p terms to zero ensures the order of accuracy of p and renders a set of equations which can be solved for the coefficients β_i with $i = 0, 1, 2, ..., p-1$. This procedure is implemented in symbolic mathematical software and results in the expressions for β_i summarised in Table 1.

Hence, by using Equation (13) and Table 1, the parameters α, β_i and γ can be expressed exclusively in terms of ρ_∞, such that the order of accuracy of the scheme is equal to p and user controlled high frequency damping is enabled. The parameter ρ_∞ remains as the only free parameter. In anticipation of Remark 2.2 below, the family of time integration schemes given by Equations (5) to (8)

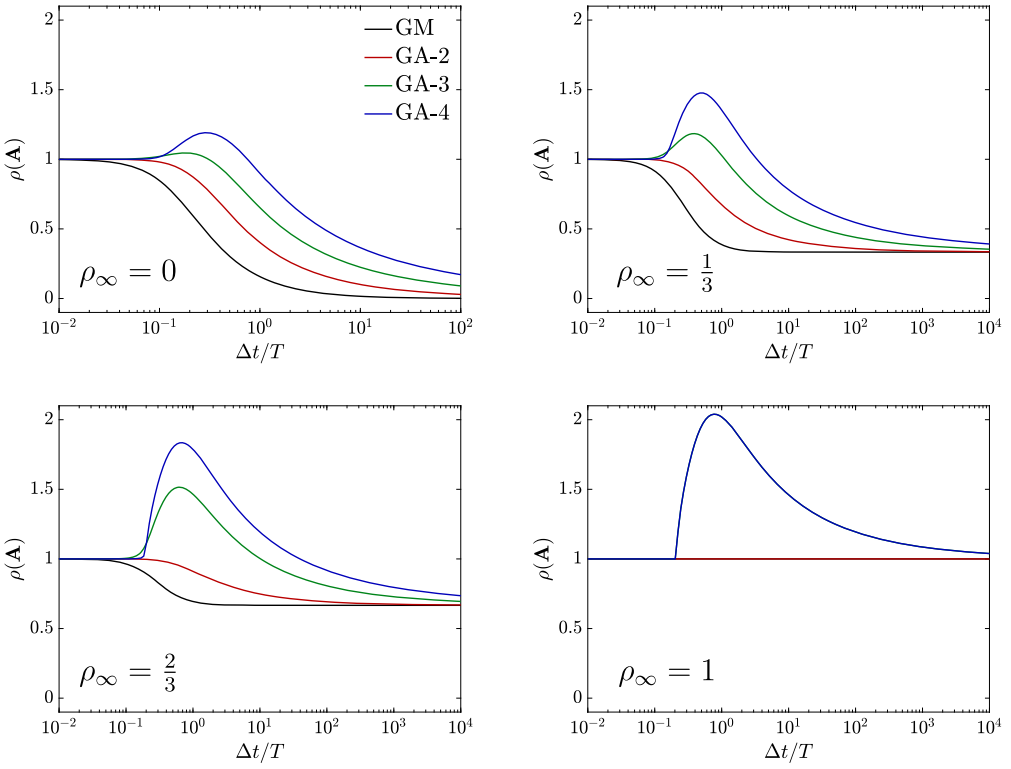

Fig. 2. Spectral radii of GM, GA-2, GA-3 and GA-4 for $\xi = 0$; for $\rho_\infty = 1$, GM and GA-3 coincide with, respectively, GA-2 and GA-4. (For interpretation of the colours in the figure(s), the reader is referred to the web version of this article.)

is termed *generalised-α method of order p*, or briefly, GA-*p*. The variation of the spectral radius $\rho(\mathbf{A}^{(p)})$ with the time step size Δt is visualised in Fig. 2. It illustrates that the scheme is unconditionally stable only for $p = 2$.

Remark 2.1. As presented by Equations (5) to (8), the scheme is not suitable for $p = 1$. An unconditionally stable first order scheme, namely the generalised midpoint rule GM, is obtained by setting $p = 1$ and $\gamma = 1$, see for instance [9]. With $\rho_\infty = 0$ and $\rho_\infty = 1$, respectively, the backward Euler and the trapezoidal rule methods are recovered. For convenience, the scheme GM is summarised in Box 1.

Remark 2.2. For $p = 2$, the scheme coincides with the popular generalised-α method proposed in [14]. If α, β_0 and β_1 are replaced, respectively, by α_f, α_m and $1 - \alpha_m$, the notation from [14] is recovered. For convenience, the scheme GA-2 is summarised in Box 2.

Remark 2.3. For $\rho_\infty = 0$, the proposed family of schemes is identical to the well-known backward difference formulae of order p. This is further elaborated in Section 5.

$$
\begin{aligned}
&\dot{u}_{n+\alpha} - f\left(u_{n+\alpha}, t_{n+\alpha}\right) = 0 \\
&u_{n+\alpha} = \alpha\, u_{n+1} + (1-\alpha)\, u_n \\
&\dot{u}_{n+\alpha} = \frac{u_{n+1} - u_n}{\Delta t} \\
&\alpha = \frac{1}{1+\rho_\infty}
\end{aligned}
$$

Box 1: Summary of the generalised midpoint rule method GM.

$$
\begin{aligned}
&\dot{u}_{n+\beta} - f\left(u_{n+\alpha}, t_{n+\alpha}\right) = 0 \\
&u_{n+\alpha} = \alpha\, u_{n+1} + (1-\alpha)\, u_n \\
&\dot{u}_{n+\beta} = \beta\, \dot{u}_{n+1} + (1-\beta)\, \dot{u}_n \\
&u_{n+1} = u_n + \Delta t \left(\gamma\, \dot{u}_{n+1} + (1-\gamma)\, \dot{u}_n\right) \\
&\alpha = \gamma = \frac{1}{1+\rho_\infty}\,, \quad \beta = \frac{3-\rho_\infty}{2(1+\rho_\infty)}
\end{aligned}
$$

Box 2: Summary of method GA-2 (equivalent to the generalised-α method).

3. Ensuring unconditional stability

The method GA-p described in Section 2 is unconditionally stable only for $p = 2$. Yet, in order to improve the accuracy while maintaining unconditional stability the following variation of Equation (5) is considered

$$\delta_3\, \dot{u}^{(3)}_{n+\beta} + (1-\delta_3)\, \dot{u}^{(2)}_{n+\beta} - \lambda\, u_{n+\alpha} = 0\,, \tag{14}$$

where $\dot{u}^{(j)}_{n+\beta}$ is defined by Equation (7) with $p = j$. The coefficients β_i in Equation (7) are given in Table 1 and also need to be selected for $p = j$. Equation (14) represents the linear combination of the GA-2 and GA-3 schemes: For $\delta_3 = 0$ the scheme reduces to GA-2 and is unconditionally stable, while for $\delta_3 = 1$ it recovers GA-3 and is more accurate but only conditionally stable. Clearly, it is desirable to find the largest possible value for $\delta_3 \geq 0$ that still ensures unconditional stability.

The Jury Table, see for instance [25], offers a suitable tool for this investigation. The analysis is tedious and results in long expressions. It is therefore most easily done using symbolic mathematical software and omitted here for the sake of brevity. The critical value of δ_3 is obtained as a function of ρ_∞, *i.e.*

$$\delta_3 = \frac{(1-\rho_\infty)^2}{2\,(1-\rho_\infty+\rho_\infty^2)}\,. \tag{15}$$

For $\rho_\infty = 0$, one obtains $\delta_3 = \frac{1}{2}$ which corresponds to an equal weighting of the second and third order accurate terms. As ρ_∞ is increased and approaches the value of 1, the weighting of GA-3 decreases and the method eventually recovers the trapezoidal rule. In the remainder of this work, the time integration scheme described by Equations (14), (6), (7), (8), (13) and (15), together with the relevant expressions from Table 1, is referred to as GA-23. The full set of equations describing GA-23 is summarised in Box 3.

$$
\begin{aligned}
&\dot{u}_{n+\beta} - f\left(u_{n+\alpha}, t_{n+\alpha}\right) = 0 \\
&u_{n+\alpha} = \alpha\, u_{n+1} + (1-\alpha)\, u_n \\
&\dot{u}_{n+\beta} = \beta_0\, \dot{u}_{n+1} + \beta_1\, \dot{u}_n + \beta_2\, \ddot{u}_n\, \Delta t \\
&u^{(i)'}_{n+1} = u^{(i)'}_n + \Delta t \left(\gamma\, u^{(i+1)'}_{n+1} + (1-\gamma)\, u^{(i+1)'}_n\right) \quad \text{for} \quad i = 0, 1 \\
&\alpha = \gamma = \frac{1}{1+\rho_\infty}\,, \quad \beta_0 = \frac{10 - 5\rho_\infty + \rho_\infty^2}{6(1+\rho_\infty)} \\
&\beta_1 = 1 - \beta_0\,, \quad \beta_2 = -\frac{(1-\rho_\infty)^2}{6(1+\rho_\infty)}
\end{aligned}
$$

Box 3: Summary of method GA-23. The coefficients β_i have been redefined for brevity of presentation.

Linear combinations of further higher order terms can also be investigated. Consider

$$\delta_4\, \dot{u}^{(4)}_{n+\beta} + (1-\delta_4)\left(\delta_3\, \dot{u}^{(3)}_{n+\beta} + (1-\delta_3)\, \dot{u}^{(2)}_{n+\beta}\right) - \lambda\, u_{n+\alpha} = 0\,, \tag{16}$$

which is the linear combination of GA-23 and GA-4. Again, the Jury Table is used to find the critical value for δ_4. The investigation renders

$$\delta_4 = \frac{(1-\rho_\infty)^2}{5\,(1+\rho_\infty^2)}\,. \tag{17}$$

For $\rho_\infty = 1$, one obtains $\delta_4 = \delta_3 = 0$ and the scheme reduces to the trapezoidal rule. For $\rho_\infty = 0$, the weighting factors for GA-2, GA-3 and GA-4 are, respectively, $\frac{2}{5}$, $\frac{2}{5}$ and $\frac{1}{5}$. Hence, the contribution of GA-4 is significant, but smaller than that of GA-3. The scheme based on Equation (16) is referred to as GA-234. The full set of equations describing GA-234 is summarised in Box 4.

$$
\begin{aligned}
&\dot{u}_{n+\beta} \;-\; f\left(u_{n+\alpha}, t_{n+\alpha}\right) \;=\; 0 \\
&u_{n+\alpha} = \alpha\, u_{n+1} + (1-\alpha)\, u_n \\
&\dot{u}_{n+\beta} = \beta_0\, \dot{u}_{n+1} + \beta_1\, \dot{u}_n + \beta_2\, \ddot{u}_n\, \Delta t + \beta_3 \ddot{u}_n\, \Delta t^2 \\
&u_{n+1}^{(i)'} \;=\; u_n^{(i)'} \;+\; \Delta t \left(\gamma\, u_{n+1}^{(i+1)'} \;+\; (1-\gamma)\, u_n^{(i+1)'}\right) \quad \text{for} \quad i = 0, 1, 2 \\
&\alpha = \gamma = \frac{1}{1+\rho_\infty}\,, \quad \beta_0 = \frac{35 - 21\rho_\infty + 7\rho_\infty^2 - \rho_\infty^3}{20(1+\rho_\infty)} \\
&\beta_1 = 1 - \beta_0\,, \quad \beta_2 = -\frac{(1-\rho_\infty)^2(5-\rho_\infty)}{20(1+\rho_\infty)}\,, \quad \beta_3 = -\frac{(1-\rho_\infty)^3}{20(1+\rho_\infty)^2}
\end{aligned}
$$

Box 4: Summary of method GA-234. The coefficients β_i have been redefined for brevity of presentation.

The investigation of unconditionally stable linear combinations of schemes GA-p including those with $p > 4$ is omitted. If they exist, they will provide little benefit due to very small weighting factors of the higher order schemes. The remainder of this article is therefore restricted to the consideration of the schemes GA-23 and GA-234.

4. Analysis of the methods GA-23 and GA-234

4.1. Stability

As described in Section 3, the schemes GA-23 and GA-234 have been derived on the basis of the Jury table and are provably unconditionally stable. The stability regions are shown in Fig. 3 and illustrate the unconditional stability. The figures show how the stability regions evolve as ρ_∞ changes from zero to one. In anticipation of Section 5, it is noted that, for $\rho_\infty = 0$, the schemes GA-p coincide with the BDF-p methods and therefore render the well-known stability regions shown in the first row of the figure for GA-2, GA-3 and GA-4. The eigenvalues of the amplification matrices of the schemes are shown in the complex plane in Fig. 4. The figure illustrates how the methods evolve as higher order terms are included or ρ_∞ is changed.

4.2. High frequency damping

Fig. 5 shows the spectral radius of the amplification matrices displayed against the time step size. Clearly, in comparison to the original generalised-α method GA-2, the proposed schemes GA-23 and GA-234 shift the onset of noticeable numerical damping to larger time steps where $\Delta t/T \approx 0.1$. It is observed that the shift from GA-2 to GA-234 is almost as significant as the shift from the generalised midpoint rule GM to the generalised-α method GA-2. Hence, GA-23 and GA-234 exhibit noticeably less numerical damping than GA-2 in the regime of large time steps that are still small enough to resolve the temporal features of the solution.

4.3. Accuracy

In order to assess the accuracy of GA-23 and GA-234 in terms of dispersion and damping, the numerical counterparts ω^h and ξ^h of, respectively, ω and ξ are considered. They can be obtained from

$$
\omega^h = \frac{1}{\Delta t}\, \arg(\zeta_{\max}) \qquad \text{and} \qquad \xi^h = -\frac{1}{\Delta t}\, \ln\left(|\zeta_{\max}|\right)\,, \tag{18}
$$

where $\zeta_{\max}$ is the maximum eigenvalue of the amplification matrix. Figs. 6 and 7 show how ω^h and ξ^h evolve with the time step size Δt. It is observed that, as expected, GA-23 exhibits smaller approximation errors than GA-2, but is less accurate than GA-234. The good performance of GA-234 is particularly noticeable when comparing the damping behaviour against the schemes GA-2 and TR.

4.4. Computational cost

In comparison to the generalised-α method GA-2, the schemes GA-23 and GA-234 require that, respectively, one or two additional history data arrays are allocated and used to store $\ddot{u}_n$ and $\dddot{u}_n$. Hence, the additional memory requirements are small, especially when compared to the amount of storage required by the global system solver. The additional computational time is similarly negligible since the additional operations are restricted to updating the global arrays $\ddot{u}_n$ and $\dddot{u}_n$.

5. Backward difference formulae

For $\rho_\infty = 0$, the time integration schemes GA-p described by Equations (5) to (8) are equivalent to the well-known backward difference formulae BDF-p, described for instance in [24]. In order to show this, Equation (8) is rewritten as

$$
u_{n+1}^{(i+1)'} \;=\; \frac{u_{n+1}^{(i)'} - u_n^{(i)'}}{\Delta t}\,, \tag{19}
$$

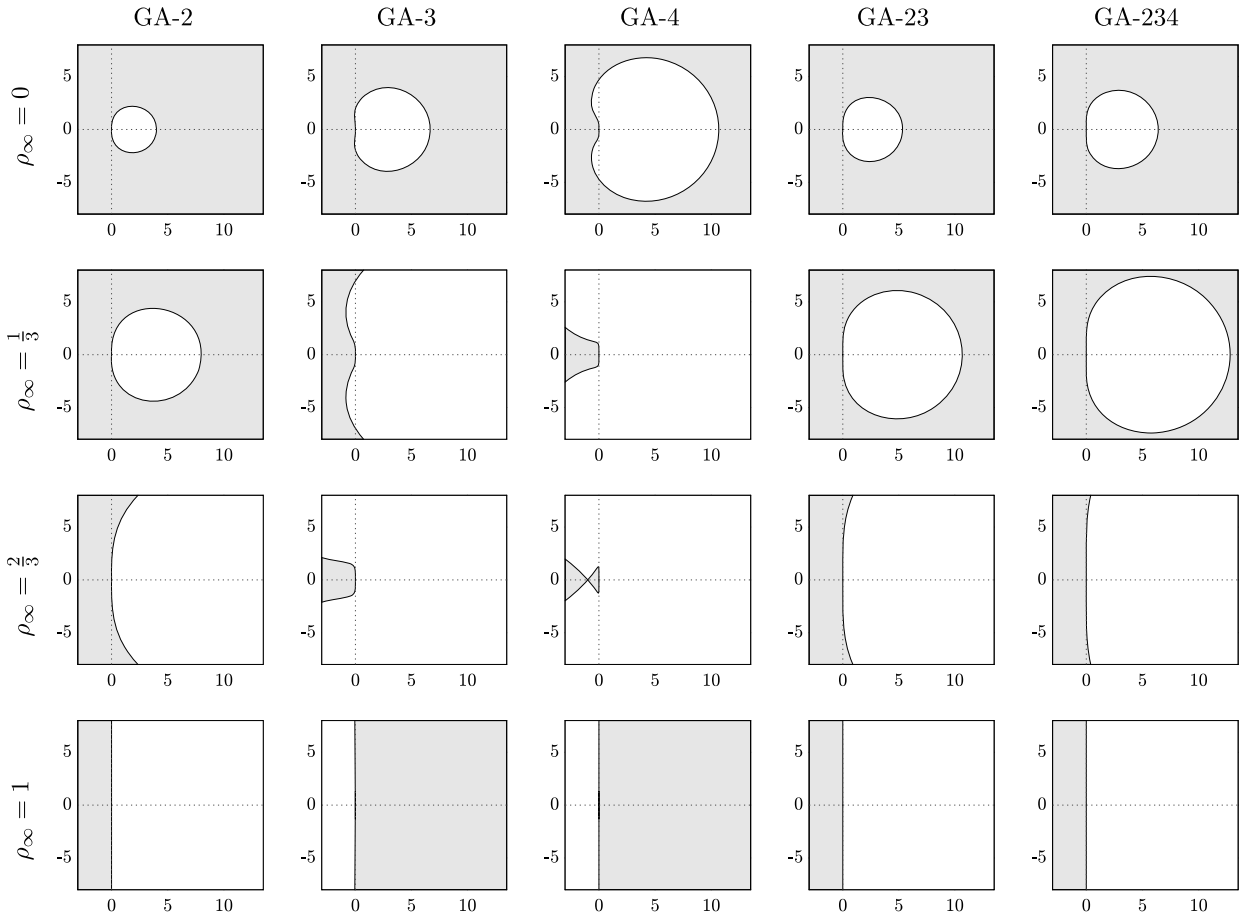

Fig. 3. Stability regions (grey), uniform scaling, $\mathrm{Im}(\lambda\Delta t)$ displayed over $\mathrm{Re}(\lambda\Delta t)$.

Table 2
Coefficients β_i for backward difference formulae BDF-p.

p	β_0	β_1	β_2	β_3	β_4
1	1	−1			
2	$\frac{3}{2}$	−2	$\frac{1}{2}$		
3	$\frac{11}{6}$	−3	$\frac{3}{2}$	$-\frac{1}{3}$	
4	$\frac{25}{12}$	−4	3	$-\frac{4}{3}$	$\frac{1}{4}$

where $\gamma = 1$ due to $\rho_\infty = 0$. This formula can be applied recursively to each term on its right-hand-side, thereby reducing the order of the derivatives and involving terms from earlier time instants. Eventually all derivatives on the right-hand-side of Equation (7) can be expressed in terms of historic values of the primary variable u and the backward difference formula is obtained. The BDF-p schemes can be expressed as

$$\dot{u}_{n+1} - \lambda u_{n+1} = 0 \tag{20}$$

$$\dot{u}_{n+1} = \frac{1}{\Delta t}\sum_{i=0}^{p} \beta_i u_{n+1-i}\,, \tag{21}$$

where the coefficients β_i are given in Table 2. The same procedure can be applied to the methods GA-23 and GA-234, resulting in linear combinations of BDF-2, BDF-3 and BDF-4. The resulting methods are denoted as BDF-23 and BDF-234 and are summarised in Boxes 5 and 6, respectively. Their numerical properties are identical to those of GA-23 and GA-234 for $\rho_\infty = 0$ and are therefore represented in the respective diagrams of Figs. 3 to 7. For convenience, the stability regions of the BDF schemes are shown together in Fig. 8. For linear problems and given the correct initial conditions, they render numerical results which are exactly equal to those

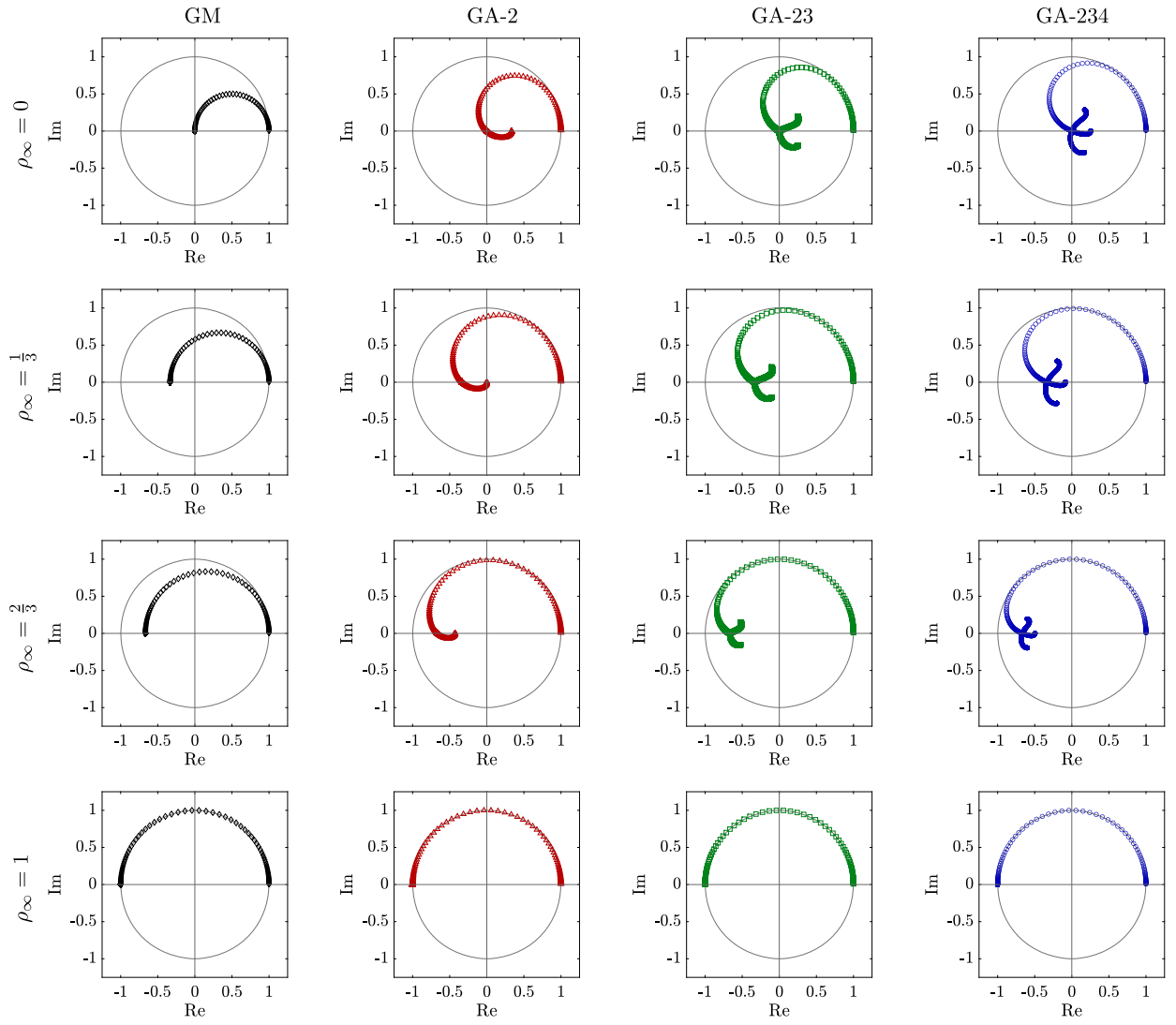

Fig. 4. Eigenvalues of the amplification matrices for $\xi = 0$, displayed in the complex plane for a range of time step sizes Δt.

obtained from GA-23 and GA-234 with $\rho_\infty = 0$. Due to this equivalence, BDF-23 and BDF-234 are not mentioned explicitly in the numerical examples in Sections 6 to 8, but are represented by their counterparts GA-23 and GA-234 with $\rho_\infty = 0$.

As opposed to GA-23 and GA-234, the schemes BDF-23 and BDF-234 do not allow for varying time step sizes or for user controlled high frequency damping. However, their implementation in any existing computer code based on BDF-1 (backward Euler) or BDF-2 is trivial and renders an immediate benefit in terms of improved accuracy.

Remark 5.1. It is noted that BDF-23 (and therefore GA-23 for $\rho_\infty = 0$) is identical to Park's method and to the BDF2OPT(4) scheme described in [13] and [26], respectively. Hence, it emerges that GA-23 corresponds to an interpolation between Park's method and the trapezoidal rule as illustrated in Fig. 1. Park's method is regarded as particularly useful for stiff problems in structural dynamics as argued in [23].

Remark 5.2. BDF-234 exceeds the accuracy of BDF-23, while it maintains its stability properties. Similarly to BDF-234, the BDF2OPT(5) scheme investigated in [26] represents the linear combination of BDF-2, BDF-3 and BDF-4. However, the stability region of BDFOPT(5) is non-convex and touches the imaginary axis in three points. It is shown in [26] that this feature can jeopardise the long-term stability of numerical simulations. The stability region of BDF-234 touches the imaginary axis only in the origin.

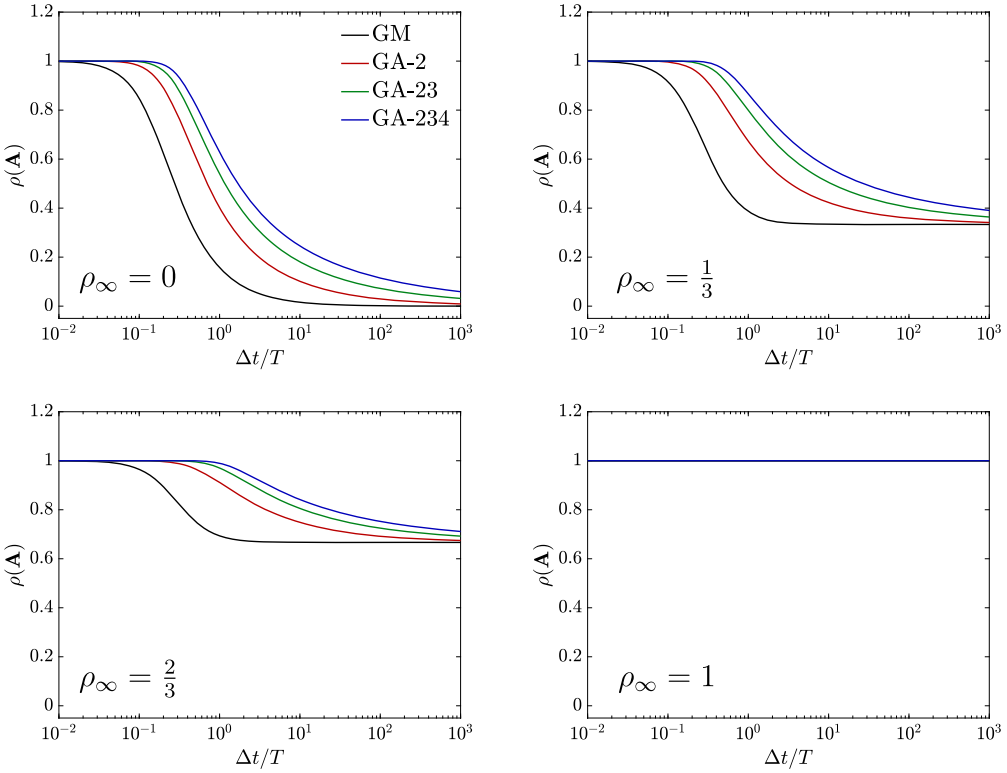

Fig. 5. Spectral radii of GM, GA-2, GA-23 and GA-234 for $\omega = 1$ and $\xi = 0$.

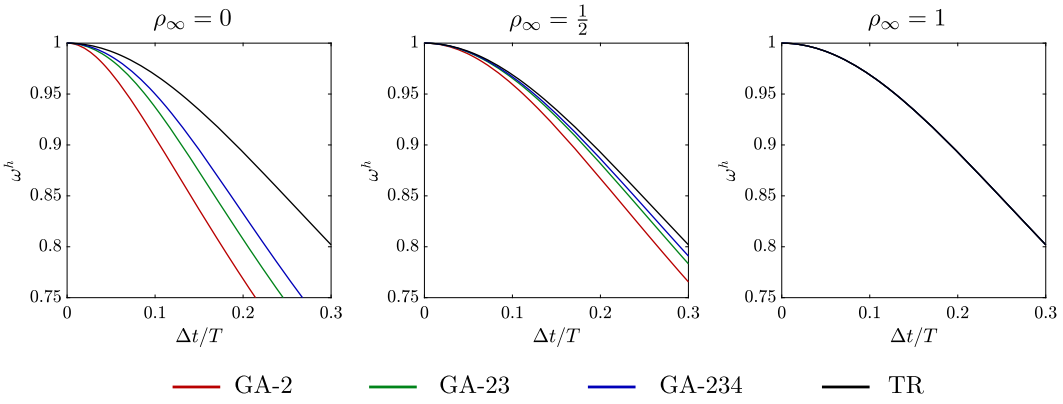

Fig. 6. Accuracy; frequency ω^h for $\omega = 1$ and $\xi = 0$.

$$\dot{u}_{n+1} - f\left(u_{n+1}, t_{n+1}\right) = 0$$
$$\dot{u}_{n+1} = \frac{10\,u_{n+1} - 15\,u_n + 6\,u_{n-1} - u_{n-2}}{6\,\Delta t}$$

Box 5: Summary of method BDF-23 (equivalent to Park's method).

$$\dot{u}_{n+1} - f\left(u_{n+1}, t_{n+1}\right) = 0$$
$$\dot{u}_{n+1} = \frac{35\,u_{n+1} - 56\,u_n + 28\,u_{n-1} - 8\,u_{n-2} + u_{n-3}}{20\,\Delta t}$$

Box 6: Summary of method BDF-234.

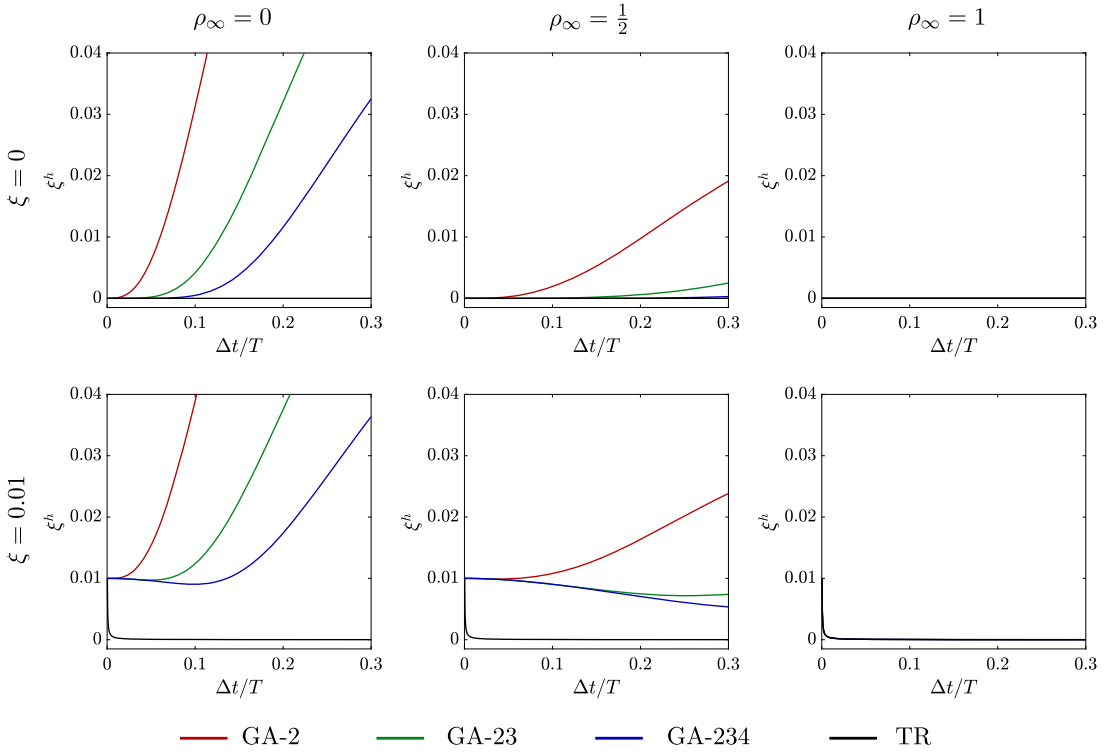

Fig. 7. Accuracy; damping coefficient ξ^h for $\omega = 1$ and different values of ξ.

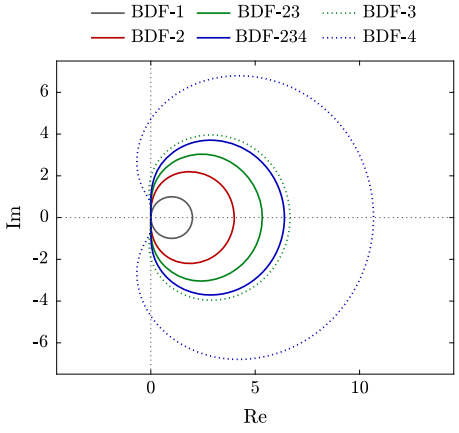

Fig. 8. Stability regions for BDF schemes.

6. Example 1: linear model problem

The standard scalar linear initial value problem described by Equation (2) is used to compare the performance of the methods presented in the preceding sections. The exact solution is given in Equation (3). The frequency is set to $\omega = 1$ and the damping factor is $\xi = 0$. Hence, the oscillation period is $T = 2\pi$. The initial condition considered is $u(0) = 1 + 0i$.

The results obtained with GA-2, GA-23 and GA-234 for different time step sizes and different values of ρ_∞ are displayed in Fig. 9. The figure shows the real part of the numerical solutions. The evolution of the imaginary part is phase shifted but qualitatively and quantitatively similar and therefore not presented for the sake of brevity.

The following observations are made from Fig. 9:

1. The solutions deviate less for $\rho_\infty = 1/3$ than for $\rho_\infty = 0$. This agrees with the fact that all schemes considered recover the trapezoidal rule for $\rho_\infty = 1$.

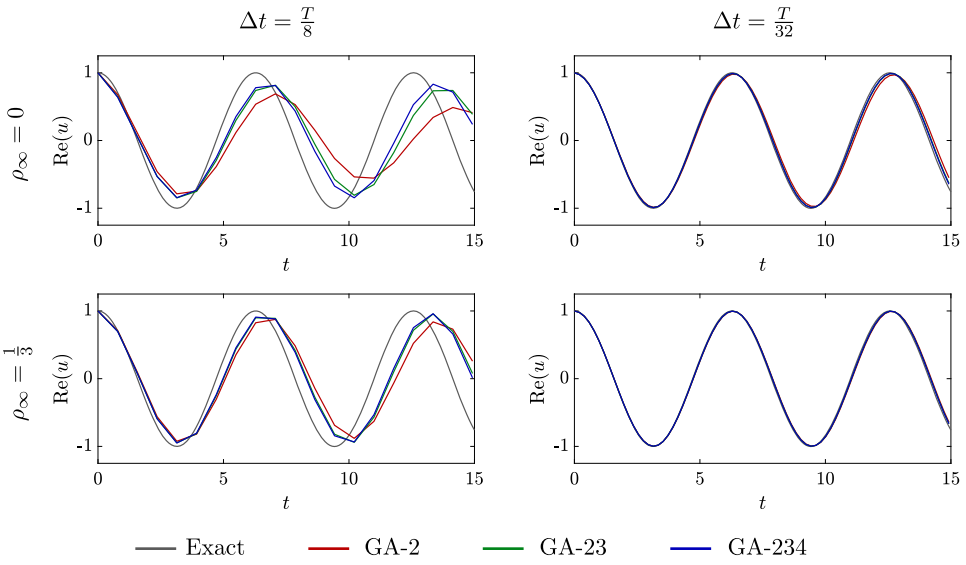

Fig. 9. Linear model problem; response obtained for $\omega = 1$ and $\xi = 0.0$.

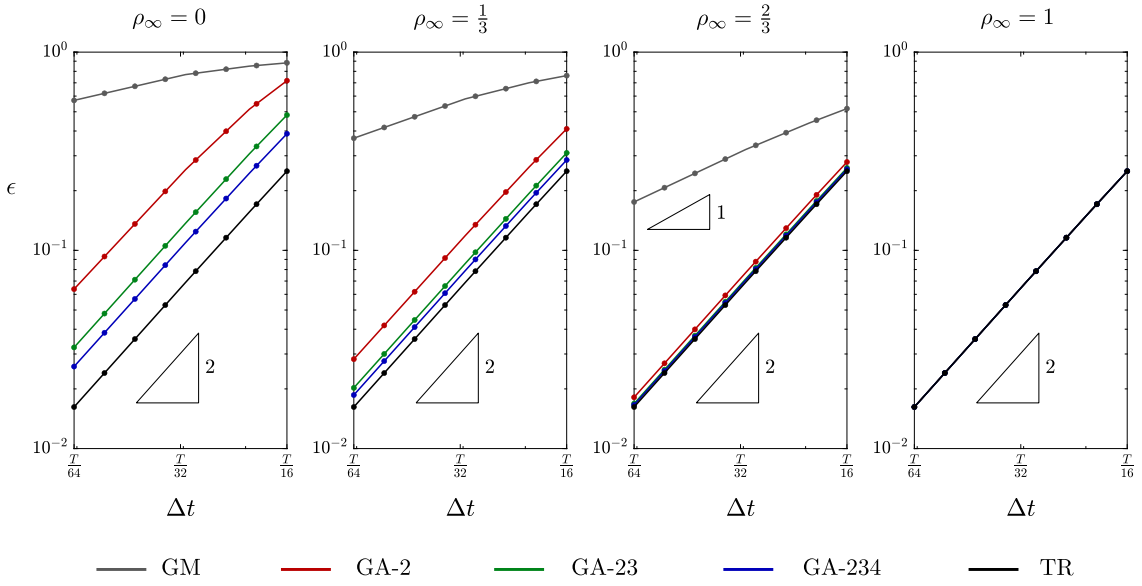

Fig. 10. Linear model problem; convergence rates.

2. For large time steps, the methods GA-23 and GA-234 are noticeably more accurate than the generalised-α method GA-2. GA-23 and GA-234 exhibit less numerical damping and a smaller frequency error. GA-234 is more accurate than GA-23.

Fig. 10 shows the convergence of the numerical solution as Δt decreases for GM, GA-2, GA-23, and GA-234 for different values of ρ_∞. The error is computed by comparing the exact solution from Equation (3), denoted here by $\tilde{u}$, to the numerical solution obtained from each method, *i.e.*

$$\epsilon = \sqrt{\frac{1}{N}\sum_{n=1}^{N} |u_n - \tilde{u}_n|^2} \tag{22}$$

where N is the number of time steps used in the respective computation to reach $t_N = 35$.

The following observations are made from Fig. 10:

3. The difference between the graphs for GA-2, GA-23 and GA-234 reduces as ρ_∞ approaches the value of one. The graphs coincide for $\rho_\infty = 1$ where all schemes recover the trapezoidal rule.

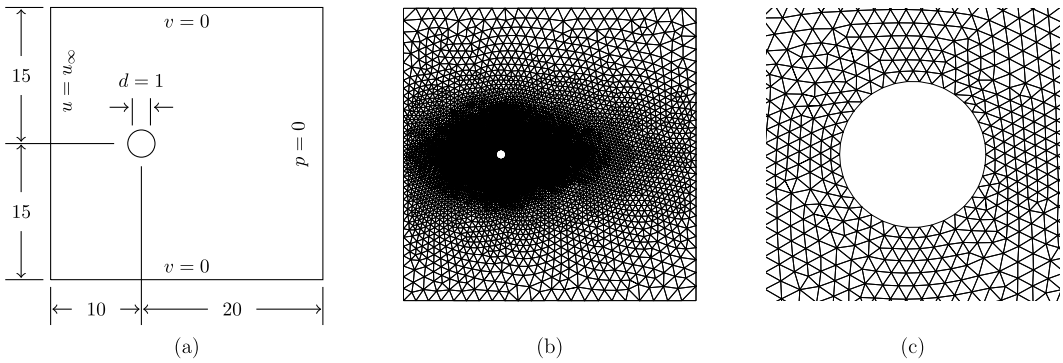

Fig. 11. Flow around cylinder; geometry and boundary conditions (a); finite element mesh (b), mesh refinement around the cylinder (c).

4. GA-23 and GA-234 render smaller approximation errors than GA-2. The accuracy level of GA-234 is closer to that of the trapezoidal rule TR than to GA-2.
5. For $\rho_\infty = 0$, the improvement in accuracy from GA-2 to GA-234 in the regime of time steps around $\Delta t = T/32$ is similar to that from the first order accurate method GM to the second order accurate scheme GA-2. This is also reflected in Fig. 9 where, for $\rho_\infty = 0$, GA-234 renders significantly more accurate results than GA-2.

Importantly, Observation 5 suggests that, in the range of time steps $T/50 < \Delta t < T/25$ which, in the context of implicit time integration, is highly relevant for industrial applications, the scheme GA-234 offers a substantial performance gain over the standard generalised-α method GA-2. Due to the equivalence between BDF-2 and GA-2 and between BDF-234 and GA-234, for $\rho_\infty = 0$, this also proves the advantage of BDF-234 over the standard method BDF-2.

7. Example 2: flow around cylinder

This benchmark example examines the flow of an incompressible fluid around a stationary circular cylinder. The flow is governed by the incompressible Navier-Stokes equations. Fig. 11 shows the geometry, boundary conditions and the employed finite element mesh consisting of 12,258 elements. The spatial discretisation is based on P2/P1 Taylor-Hood velocity-pressure elements (quadratic velocity and linear pressure interpolation), see for instance [28]. The convective velocity is approximated with second order accuracy as described in [18], which results in a linear global equation system that is solved in every time step for the velocity and the pressure degrees of freedom. The total number of degrees of freedom is 55,138. The vertical velocity component v is set to zero at the upper and lower boundaries, while the horizontal velocity component u remains unconstrained. In addition, the pressure at the outlet boundary is set to zero and, at the inlet boundary, u is prescribed uniformly as $u_\infty = 1$. The cylinder diameter is $d = 1$, while the fluid density and viscosity are given by $\rho = 1$ and $\mu = 0.01$, respectively. Hence, the Reynolds number is $Re = \rho u_\infty d/\mu = 100$. The Strouhal number St is defined as

$$St = \frac{f d}{u_\infty} \tag{23}$$

where f is the frequency of the vortex shedding, *i.e.* the frequency of the oscillation of the lift force on the cylinder. The flow is simulated with the schemes GM, GA-2, GA-23, and GA-234.

Fig. 12 illustrates the evolution of the drag and lift coefficients over time. Fig. 13 shows the convergence of the Strouhal number as the time step size Δt is reduced. Clearly, as Δt is reduced, all methods converge to $St = 0.1728$. This value depends on the Reynolds number, the size of the domain and the mesh density employed. It agrees well with the results reported, for instance, in [9,18] and references therein. The convergence pattern is identical to that observed for the linear model problem in Section 6: The schemes GA-23 and GA-234 perform better than GA-2 and this is most evident for values of ρ_∞ close to zero and in the range of physically relevant time step sizes. Note that the simulation fails for the TR scheme in the regime of small time steps due to the lack of numerical damping.

8. Example 3: pulsatile flow through a cavity

Consider a two dimensional cavity with inflow and outflow channels as shown in Fig. 14(a). The inflow velocity has a quadratic profile. The peak velocity $\bar{u}_{\text{in}}$ pulsates between 0 and 8 with $\bar{u}_{\text{in}}(t) = 4\,(1 - \cos(2\pi\, t/5))$. The fluid flow is governed by the incompressible Navier-Stokes equations. The fluid density and viscosity are, respectively, $\rho = 1$ and $\eta = 0.01$. On the channel and cavity walls the non-slip boundary condition applies. The fluid domain is discretised with 7,890 P2/P1 Taylor-Hood velocity-pressure elements, resulting in a total number of degrees of freedom of 35,010. The finite element mesh is shown in Fig. 14(b). The simulation is performed with methods GA-2, GA-23 and GA-234 for $\rho_\infty = 0$ and different time step sizes. For the finite element mesh and time step sizes employed, the simulation can also be performed with the trapezoidal rule TR. All simulations are terminated at $t = 15$.

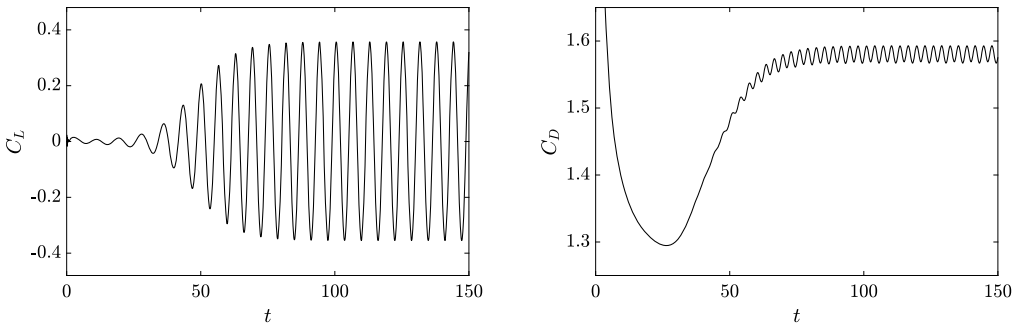

Fig. 12. Flow around cylinder; typical evolution of the lift and drag coefficients.

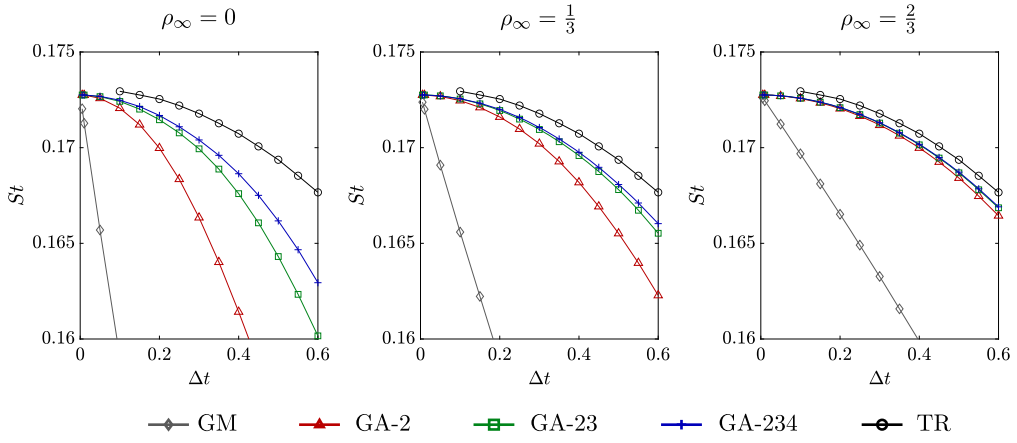

Fig. 13. Flow around cylinder; St convergence.

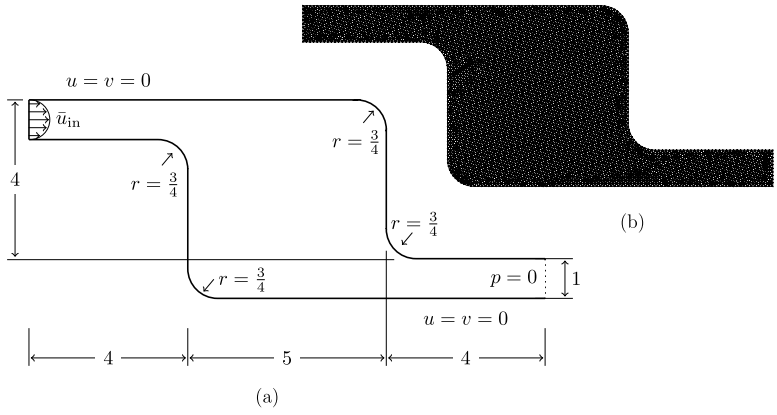

Fig. 14. Flow through a cavity; geometry and boundary conditions (a); finite element mesh (b).

Fig. 15 shows typical velocity and vorticity distributions, illustrating the vortex that forms in the cavity. Using GA-234, a reference solution at $t = 15$ with velocity field $\tilde{\boldsymbol{u}}$ is generated for $\Delta t = 0.001$. For all other solutions at $t = 15$, the approximation error is estimated by

$$\epsilon = \sqrt{\int \|\boldsymbol{u} - \tilde{\boldsymbol{u}}\|^2 \, \mathrm{d}a} \,, \tag{24}$$

where the integration is performed over all elements of the mesh. Fig. 16 shows the convergence of the error estimate to the mesh dependent reference solution. The convergence pattern confirms that GA-23 exceeds the accuracy of GA-2, while GA-234 is more accurate than GA-23 and renders errors that are almost as small as those of the TR scheme.

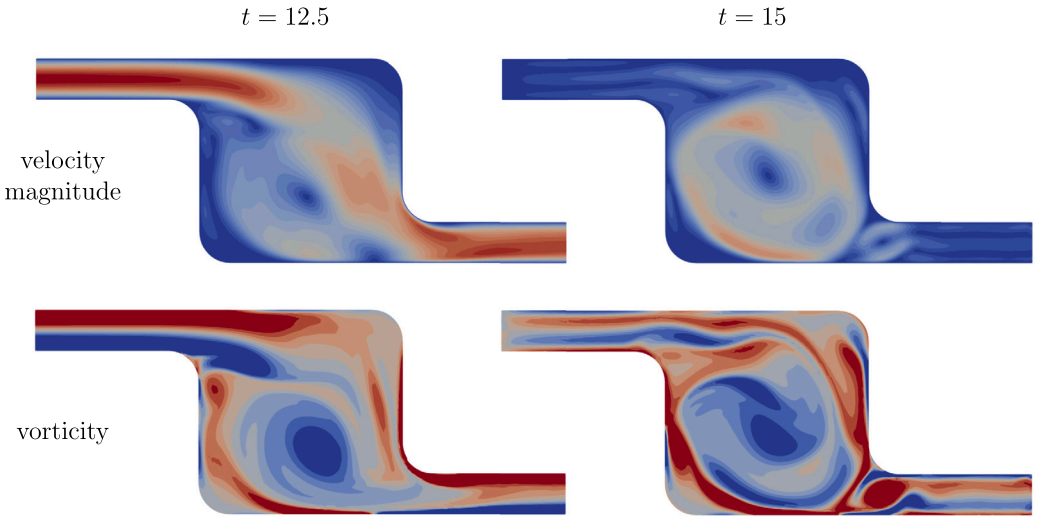

Fig. 15. Flow through a cavity; typical velocity magnitude (0 [blue] to 8 [red]) and vorticity (-10 [blue] to +10 [red]) contour plots.

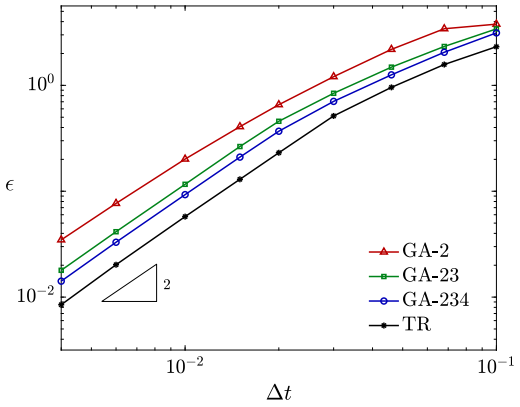

Fig. 16. Flow through a cavity; temporal convergence.

9. Conclusions

Two new time integration schemes, namely GA-23 and GA-234, have been presented. They are closely related to the well-known generalised-α method proposed in [14]. While maintaining unconditional stability and second order accuracy, they offer the same high-frequency damping control, but render smaller approximation errors. As illustrated in Fig. 1 and demonstrated in the numerical examples, the scheme GA-234 almost achieves the approximation accuracy of the trapezoidal rule, while maintaining the high frequency damping needed for the simulation of real-world applications.

It has also been shown that, for $\rho_\infty = 0$, GA-23 and GA-234 can be expressed as backward difference formulae, referred to, respectively, as BDF-23 and BDF-234. The scheme BDF-23 is equivalent to Park's method and to the BDF2OPT(4) formula, see [13] and [26], respectively. The stability regions are shown in Fig. 8.

The schemes have been derived from weighted linear combinations of extensions of the generalised-α method to higher approximation orders.

Compared to the original generalised-α method and BDF schemes, the additional computational cost associated with GA-23, GA-234, BDF-23 and BDF-234 is negligible.

CRediT authorship contribution statement

Wulf G. Dettmer: Writing – review & editing, Writing – original draft, Supervision, Software, Methodology, Investigation, Conceptualization. **Eman Alhayki:** Validation, Software, Methodology, Investigation, Formal analysis.

Declaration of competing interest

The authors declare that they have no known competing financial interests or personal relationships that could have appeared to influence the work reported in this paper.

Data availability

No data was used for the research described in the article.

References

[1] M. Ashour, N. Valizadeh, T. Rabczuk, Phase-field Navier–Stokes model for vesicle doublets hydrodynamics in incompressible fluid flow, Comput. Methods Appl. Mech. Eng. 412 (2023).
[2] K.J. Bathe, M.M.I. Baig, On a composite implicit time integration procedure for nonlinear dynamics, Comput. Struct. 83 (2005) 2513–2524.
[3] G. Bauer, P. Gamnitzer, V. Gravemeier, W.A. Wall, An isogeometric variational multiscale method for large-eddy simulation of coupled multi-ion transport in turbulent flow, J. Comput. Phys. 251 (2013) 194–208.
[4] Y. Bazilevs, V. Calo, J. Cottrell, T. Hughes, A. Reali, G. Scovazzi, Variational multiscale residual-based turbulence modeling for large eddy simulation of incompressible flows, Comput. Methods Appl. Mech. Eng. 197 (2011) 173–201.
[5] Y. Bazilevs, K. Takizawa, T.E. Tezduyar, Computational Fluid-Structure Interaction, Wiley, 2013.
[6] P. Behnoudfar, Q. Deng, V.M. Calo, Higher-order generalized-α methods for hyperbolic problems, Comput. Methods Appl. Mech. Eng. 378 (2021) 113725.
[7] J. Chung, G. Hulbert, A time integration algorithm for structural dynamics with improved numerical dissipation: the generalized-α method, J. Appl. Mech. 60 (1993) 371–375.
[8] O. Colomés, A. Main, L. Nouveau, G. Scovazzi, A weighted shifted boundary method for free surface flow problems, J. Comput. Phys. 424 (2021).
[9] W. Dettmer, D. Perić, An analysis of the time integration algorithms for the finite element solutions of incompressible Navier–Stokes equations based on a stabilised formulation, Comput. Methods Appl. Mech. Eng. 192 (2003) 1177–1226.
[10] W. Dettmer, D. Perić, A computational framework for fluid–structure interaction: finite element formulation and applications, Comput. Methods Appl. Mech. Eng. 195 (2006) 5754–5779.
[11] W. Dettmer, D. Perić, A new staggered scheme for fluid–structure interaction, Int. J. Numer. Methods Eng. 93 (2013) 1–22.
[12] H. Gómez, V. Calo, Y. Bazilevs, T. Hughes, Isogeometric analysis of the Cahn–Hilliard phase-field model, Comput. Methods Appl. Mech. Eng. 197 (2008) 4333–4352.
[13] T. Hughes, The Finite Element Method: Linear Static and Dynamic Finite Element Analysis, Prentice-Hall, 1987.
[14] K. Janssen, C. Whiting, G. Hulbert, A generalized-α method for integrating the filtered Navier–Stokes equations with a stabilized finite element method, Comput. Methods Appl. Mech. Eng. 190 (2000) 305–319.
[15] M. Joosten, W. Dettmer, D. Perić, On the temporal stability and accuracy of coupled problems with reference to fluid–structure interaction, Int. J. Numer. Methods Fluids 64 (2010) 1363–1378.
[16] C. Kadapa, W. Dettmer, D. Perić, On the advantages of using the first-order generalised-alpha scheme for structural dynamic problems, Comput. Struct. 193 (2017) 226–238.
[17] C. Kadapa, W. Dettmer, D. Perić, A stabilised immersed framework on hierarchical b-spline grids for fluid-flexible structure interaction with solid–solid contact, Comput. Methods Appl. Mech. Eng. 335 (2018) 472–489.
[18] C. Kadapa, W. Dettmer, D. Perić, Accurate iteration-free mixed-stabilised formulation for laminar incompressible Navier-Stokes: applications to fluid-structure interaction, J. Fluids Struct. 97 (2020).
[19] M. Kästner, P. Metsch, R. de Borst, Isogeometric analysis of the Cahn–Hilliard equation – a convergence study, J. Comput. Phys. 305 (2016) 360–371.
[20] C. Kees, I. Akkerman, M. Farthing, Y. Bazilevs, A conservative level set method suitable for variable-order approximations and unstructured meshes, J. Comput. Phys. 230 (2011) 4536–4558.
[21] H.J. Kim, H.C. Rundfeldt, I. Lee, S. Lee, Tissue-growth-based synthetic tree generation and perfusion simulation, Biomech. Model. Mechanobiol. 22 (2023) 1095–1112.
[22] X. Mao, R. Jaiman, An interface and geometry preserving phase-field method for fully Eulerian fluid-structure interaction, J. Comput. Phys. 476 (2023).
[23] K.C. Park, An improved stiffly stable method for direct integration of nonlinear structural dynamic equations, J. Appl. Mech. 2 (1975) 464–470.
[24] A. Quarteroni, R. Sacco, F. Saleri, Numerical Mathematics. Springer, 2000.
[25] R. Raible, A simplification of jury's tabular form, IEEE Trans. Autom. Control 19 (1974) 248–250.
[26] V.N. Vatsa, M.H. Carpenter, D.P. Lockard, Re-evaluation of an optimized second order backward difference (BDF2OPT) scheme for unsteady flow applications, in: 48th AIAA Aerospace Sciences Meeting, Jan 4-7, 2010, Orlando, FL USA, 2010.
[27] J. Vila-Cha, A.C. Carneiro, B. Ferreira, F.A. Pires, A numerical assessment of partitioned implicit methods for thermomechanical problems, Comput. Struct. (2023) 277–278.
[28] O.C. Zienkiewicz, R.L. Taylor, P. Nithiarasu, The Finite Element Method for Fluid Dynamics, 6 ed., Elsevier, 2005.